ACS APPLIED ENERGY MATERIALS

www.acsaem.org Article

Insights into the Redox Behavior of $Pr_{0.5}Ba_{0.5}MnO_{3-\delta}$-Derived Perovskites for CO_2 Valorization Technologies

Andrea Felli, Silvia Mauri, Marcello Marelli, Piero Torelli, Alessandro Trovarelli, and Marta Boaro*

Cite This: *ACS Appl. Energy Mater.* 2022, 5, 6687−6699 Read Online

ACCESS | Metrics & More | Article Recommendations | Supporting Information

ABSTRACT: *In situ* temperature-programmed (TP) analyses in a multianalytical approach including X-ray diffractometry (XRD), temperature-programmed reduction (TPR), thermogravimetry (TGA), near-edge X-ray absorption fine structure spectroscopy (NEXAFS) are used to study the relationship between redox properties and structural changes in $Pr_{0.5}Ba_{0.5}MnO_{3-\delta}$ (*m*-PBM), $PrBaMn_2O_{5+\delta}$ (*r*-PBM), and $PrBaMn_2O_{6-\delta}$ (*o*-PBM) when exposed to reduction/oxidation cycles. TP-XRD analysis shows that under reducing conditions, between 300 and 850 °C, the biphase perovskite *m*-PBM turns into the monolayered perovskite *r*-PBM. Stabilization of the latter phase at room temperature requires early oxidation in air at a high temperature (850 °C) to avoid segregation, resulting in the formation of the oxidized layered phase (*o*-PBM). The *o*-PBM layered perovskite is characterized by the H_2-TPR profile, showing two reduction peaks at temperatures below 500 °C. TP-NEXAFS characterization reveals the copresence of Mn(IV) (60%), Mn(III) (30%), and Mn(II) (10%) and helps to interpret the reduction profile: Mn(IV) converts to Mn(III) at ∼300 °C (I pk), Mn(III) to Mn(II) at ∼450 °C (II pk). The TGA characterization confirms the reversibility of the *o*-PBM ↔ *r*-PBM process at 800 °C; in addition, it shows that the *r*-PBM can be oxidized almost completely (∼99%) also by CO_2 without accumulation of carbonates. This study sheds light on the peculiar redox behavior of PBM-based materials and paves the way for their application as oxygen carriers and catalytic promoters in different CO_2 enhancement technologies. Here, we discuss the results obtained to develop versatile and redox-resistant electrodes for solid oxide electrochemical cell/solid oxide fuel cell applications.

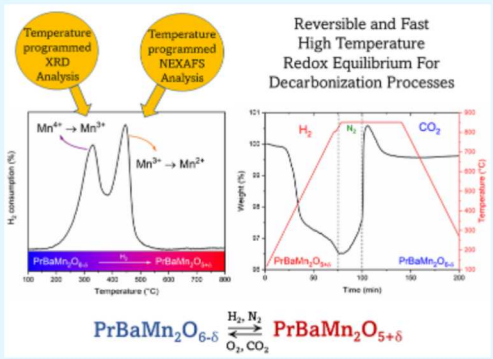

KEYWORDS: *solid oxide fuel cell, CO_2 electrolysis, double layered perovskites, redox behavior, temperature-programmed analysis, NEXAFS*

Downloaded via UNIV DEGLI STUDI DI UDINE on August 3, 2022 at 12:07:06 (UTC).
See https://pubs.acs.org/sharingguidelines for options on how to legitimately share published articles.

INTRODUCTION

In the past decades, the necessity for sustainable development and greenhouse gas abatement led to continuous technological advances in low-carbon-emission energy conversion tecnologies.[1,2] Electrochemical technologies (fuel cells and electrolyzers), based on the use of renewable resources and CO_2 valorization, have a growing importance in the present energy transition.[3] In particular, solid oxide fuel cells (SOFCs), which work with H_2 but also with traditional fuels, constitute an ideal bridging technology.[4] These systems directly convert the chemical energy of fuels into electrical power, combining high energy conversion efficiency with great fuel flexibility[5,6] and decreased emissions, producing electricity and heat at the same time.[7] The competitiveness of this technology compared to traditional technology requires decreasing production costs and extending the lifetime of devices. Several R&D efforts are focusing on the identification and implementation of durable, low-cost materials that enable the engineering of systems that operate at a lower temperature,[8−10] in a reversible manner[11−13] (i.e., also functioning as electrolyzers), and that can be easily manufactured. In this perspective, the development of symmetric cells (with equal fuel and oxygen electrodes) would lead to great advantages.[11,14] The electrode materials for these advanced devices must not only have better mixed electronic−ionic conductivity but also high stability and flexibility to work in different reaction atmospheres, i.e., they must have adequate redox properties. A better understanding of the correlations between structural changes, redox properties, and electrocatalytic properties of materials is therefore crucial for progresses in this field. Perovskite oxides and related structures (double perovskites and layered perovskites) show a high compositional and structural flexibility[15] and have found application in heterogeneous catalysis[16] and energy conversion applications[17−20] thanks to the possibility of tuning functional properties (conductivity and catalytic and electrocatalytic

Received: January 17, 2022
Accepted: May 4, 2022
Published: May 18, 2022

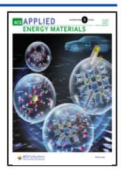

© 2022 The Authors. Published by American Chemical Society

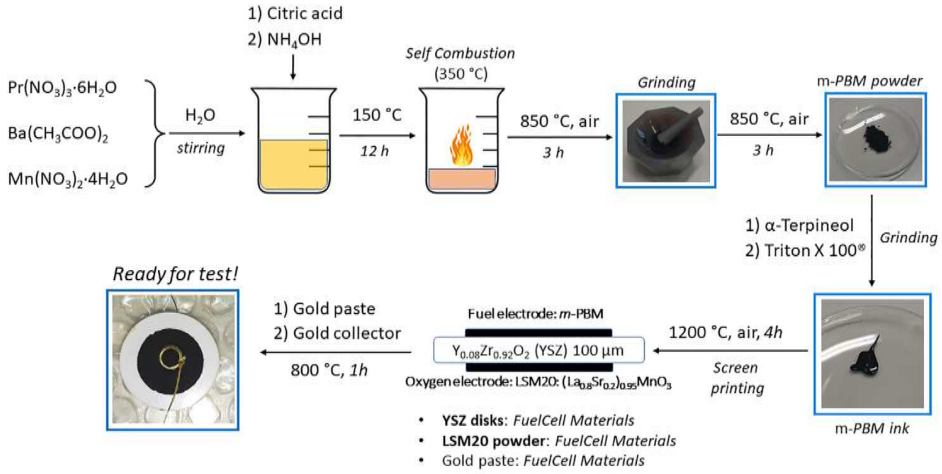

Figure 1. Scheme of the preparation of $Pr_{0.5}Ba_{0.5}MnO_3$ (*m*-PBM) and of the *m*-PBM//YSZ//LSM button cell.

activity) by properly doping A and B sites[21] and through exsolution of incorporated dopants.[22,23]

In the field of solid oxide electrochemical cells (SOECs), perovskite has been shown to satisfy better than other more conventional cermet materials the requirement of redox stability and reversibility. Several perovskite oxides are able to preserve their structure after numerous redox cycles, and moreover, they show a high mixed ionic and electronic conductivity (MIEC) in both oxidizing and reducing atmospheres.[11,24−27] Recently, Pr and Ba double layered perovskites were proposed as promising, redox-stable electrodes for both cathodic and anodic applications in SOFCs. $PrBaCo_2O_{5+\delta}$ and $PrBaFe_2O_{5+\delta}$ were mainly (but not only) investigated as cathodic electrodes;[28−33] in 2015, Sengodan *et al.*[34,35] showed how high-temperature annealing in hydrogen enables obtainment of the high-conductivity layered perovskite $PrBaMn_2O_{5+\delta}$ from the mixed perovskite $Pr_{0.5}Ba_{0.5}MnO_3$. In reducing atmospheres, A-site Pr^{3+} and Ba^{2+} cations settle onto alternated layers, intercalated by a $[MnO_2]$ sublattice. This lattice arrangement allows for a high electronic conductivity due to the presence of Mn^{3+}/Mn^{2+} redox couples and an improved ionic conductivity related to the large number of O^{2-} vacancies through subcoordinated cation planes. This transformation increases the efficiency of anodic electrodes in SOFCs.

Most of the studies on this material have been focused on the relationship between the formation of the layered structure and the exsolution process both in SOFC applications[22,36,37] and in catalysis.[38−40] Only few studies discussed the oxygen storage capacity of a layered structure,[41,42] while no detailed studies have been published on the redox processes involved in the formation and stabilization of the layered structure, at least to the best of the authors' knowledge. In a previous study,[43] we demonstrated that the redox behavior of PBM oxides is correlated to the structural changes that they undergo during thermal reduction. This study aims to gain more insights into this relationship and to verify correlations between reduction processes and the intrinsic structural changes occurring in PBM phases. For the first time, a parallel characterization of structure rearrangement and redox cycles of these oxides has been carried out via the combination of several *in situ* temperature-programmed analysis techniques (TPR, TGA, XRD, and NEXAFS). Details on the redox processes involved in the reduction/oxidation of $PrBaMn_2O_{5+\delta}$ and $PrBaMn_2O_{6-\delta}$ layered phases were obtained. The reversibility of the cycles and versatility to different oxidizing environments (air and carbon dioxide) were also investigated underlining the endurance of these oxides to high-temperature and abrupt environmental changes.

Finally, the practical impact of our findings on the development of a new class of oxygen storage carriers for CO_2 valorization technologies was investigated in the context of SOEC/SOFC applications.

EXPERIMENTAL SECTION

Synthesis of PBM Phases. Four-gram batches of $Pr_{0.5}Ba_{0.5}MnO_{3-\delta}$ (*m*-PBM) powders were prepared by means of a sol−gel combustion route. Stoichiometric amounts of $Pr(NO_3)_3{\cdot}6H_2O$ (Treibacher Industrie AG), $Ba(CH_3COO)_2$ (Sigma-Aldrich), and $Mn(NO_3)_2{\cdot}4H_2O$ (Sigma-Aldrich) were dissolved in distilled water. Citric acid (CA, Sigma-Aldrich) was used as a complexing agent (in a 1:1 CA:cation molar ratio), and an ammonium hydroxide solution (30%, Sigma-Aldrich) was added in order to adjust the pH of the solution to 6.3. The solution was stirred and dried at 150 °C for 20 h. The obtained gel was self-ignited at 350 °C to remove most of the organic compounds and calcinated in air at 850 °C (2 °C·min^{-1}) in two steps of 3 h each. Between the first and the second calcination, the sample was ground manually for 5 min to promote a better homogeneity of the phases. $PrBaMn_2O_{6-\delta}$ (*o*-PBM) was obtained by successive annealing of *m*-PBM powders in humidified H_2 (3% H_2O) at 800 °C (10 °C·min^{-1}) for 4 h and cooling the sample in air (∼30 °C·min^{-1}). A pure layered perovskite $PrBaMn_2O_{5+\delta}$ (*r*-PBM) phase was obtained from the *o*-PBM reduction at 800 °C (10 °C·min^{-1}) in 10% H_2−90% N_2 for 15 h (cooling ramp of 30 °C·min^{-1}, in N_2).

Button Cell Preparation. $Pr_{0.5}Ba_{0.5}MnO_{3-\delta}$//$Zr_{0.92}Y_{0.08}O_2$//$(La_{0.8}Sr_{0.2})_{0.95}MnO_{3-\delta}$ electrolyte-supported button cells were prepared by screen printing using $Zr_{0.92}Y_{0.08}O_2$ electrolytes (YSZ, Fuel Cell Materials) with a diameter of 25 mm and a nominal thickness of about 300 μm. The $(La_{0.8}Sr_{0.2})_{0.95}MnO_3$ (LSM) cathode was prepared using a commercial powder (LSM20-P, Fuel Cell Materials), while *m*-PBM was used to fabricate the anode. Perovskite powders were suspended in a mixture of α-Terpineol (Sigma-Aldrich) and Triton X (70%−30% in volume, respectively), adding a small quantity of graphite (5% of total weight) to increase the porosity of the electrode. A laboratory screen printing setup was used to deposit the anodic and cathodic inks on the YSZ pellets. Both the LSM cathode and the *m*-PBM anode were sintered for 4 h at 1200 (3 °C·min^{-1}) and 1100 °C (3 °C·min^{-1}), respectively, to improve the interface adhesion between electrodes and electrolytes. Before testing, a gold grid was used as a collector on both the electrodes. Gold paste (AU-I, Fuel Cell Materials) was used to paste the grids to the electrodes. A final calcination at 800 °C (5 °C·min^{-1})

https://doi.org/10.1021/acsaem.2c00163
ACS Appl. Energy Mater. 2022, 5, 6687−6699

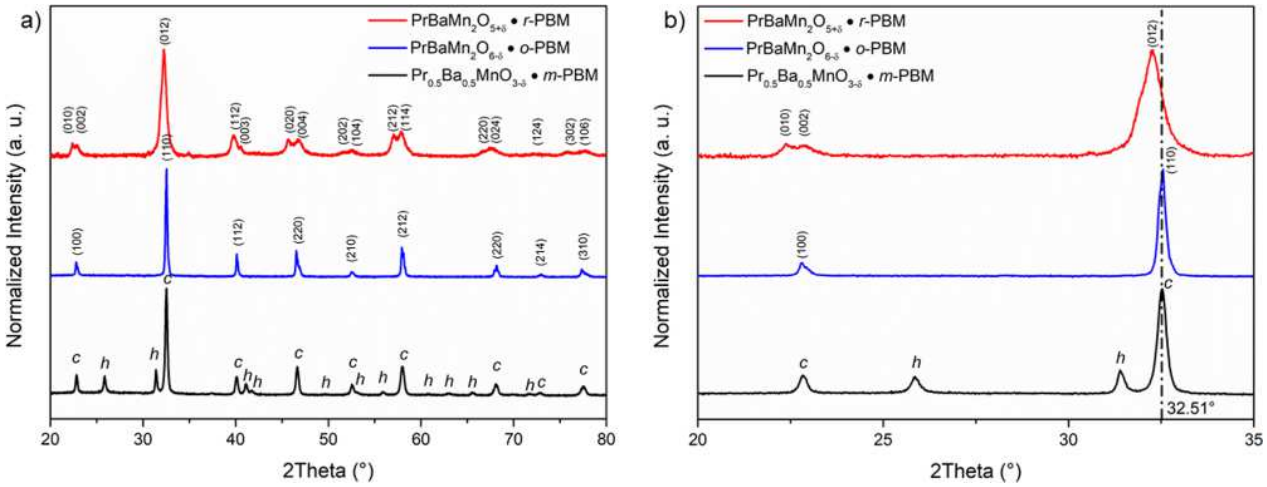

Figure 2. XRD spectra (a) of *m*-PBM ($Pr_{0.5}Ba_{0.5}MnO_{3-\delta}$, black), *o*-PBM ($PrBaMn_2O_{6-\delta}$, blue), and *r*-PBM ($PrBaMn_2O_{5+\delta}$, red); (b) magnification between 20 and 35°. c, Cubic phase. h, Hexagonal phase.

for 1 h was carried out for a well adhesion of the gold grids and to ensure good electron collection during operation.

Figure 1 summarizes the main steps of the procedure described above.

Characterization Techniques. X-ray diffraction (XRD) characterization was carried out with a Philips PW3040/60 X'Pert PRO diffractometer (Bragg–Brentano geometry), using Cu Kα radiation (40 kW, 20 mA, λ = 0.154 nm) and acquiring patterns in the 2θ range from 20 to 80°, at 0.02° steps with a counting time of 40 s·step^{-1}. The identification of the crystalline phases was done by consulting bibliographical[44−46] and online database references.[47] A stainless-steel chamber with Be windows was assembled on a spectrometer to study the phase evolution in a reductive/oxidant atmosphere at high temperatures; the spectra were acquired at 0.01° steps at a counting time of 80 s·step^{-1} in the 2θ range from 20 to 34°. This is the range that allows for observation of the reconstruction of the cubic and the hexagonal structures into the layered phase, as well as possible segregation and metastable phases. The restricted range of analysis allows us to avoid long isothermal steps and to have a better approximation of the structural modification occurring during a TPR experiment.

Temperature-programmed reductions (TPRs) were carried out consecutively in an analyzer with a thermal conductivity detector (Autochem II 2920 Micromeritics). Before cycling, the surface of the sample (50 mg of *m*-PBM) was cleaned of adsorbates by thermal treatment in air at 500 °C for 1 h. Then, the sample was purged in N_2 at room temperature (RT) and heated to 900 °C (10 °C·min^{-1}), under a constant gas flow of 4.43% H_2 in N_2 (35 mL·min^{-1}). After an isothermal step of 10 min, the sample was left to cool in air (35 mL·min^{-1}, ramp of 30 °C·min^{-1}). The procedure was repeated four times. The CO_2 oxidation and desorption were analyzed using a mass spectrometer Pfeiffer Vacuum D-35614 Asslar using a constant flow of 20% CO_2 in He (35 mL·min^{-1}). N_2 was used during the TPD analysis.

A ZEISS Libra200FE was used for transmission electron microscopy (TEM) analysis. Specimens were suspended in isopropyl alcohol and placed for 10 min in an ultrasound bath. A suspension drop was deposited onto a lacey carbon copper TEM grid and analyzed after overnight drying.

A JEOL JSM7610F Plus field-emission scanning electron microscope (FE-SEM) was used to characterize the PBM button cells before and after the electrochemical tests.

Thermogravimetric analysis (TGA) profiles were acquired using a Q500 (TA Instruments). Several redox cycles were performed on 20 mg of *m*-PBM using H_2 (2% in N_2, 100 mL·min^{-1}) as a reducing agent and air for the reoxidation of the sample. For SDT (simultaneous differential scanning calorimetry–thermogravimetry analysis), a Q600 (TA Instruments) was instead employed for a similar study, using CO_2 (20% in He, total flow rate of 100 mL·min^{-1}) as the oxidizing agent.

In situ AP-NEXAFS measurements were performed at the APE-HE beamline of "Elettra" Synchrotron, in Trieste. The beamline is equipped with an experimental setup designed to acquire NEXAFS spectra continuously at 1 bar, in the TEY mode, by using a home-made reaction cell, described in detail elsewhere.[48] Oxidizing and reducing gases (H_2 and O_2) were injected inside the cell through a gas line controlled by three flowmeters, calibrated to a maximum total flow of 50 mL·min^{-1}. Since the TEY mode is surface-sensitive (probing depth of ≈ 5 nm), the first step of the experiment involved a thermal treatment from RT to 360 °C, exposing the sample to He (50 mL·min^{-1}). After that, the temperature was decreased to RT. Then, the temperature was increased again to 370 °C, exposing the sample to a mixture of He (96%)/H_2 (4%). Once the temperature reached 370 °C and upon observing the Mn reduction, an oxidizing He (96%)/O_2 (4%) mixture was fed while decreasing the *T* to RT. The H_2/O_2 cycle was repeated twice to investigate the stability of the sample under redox conditions. During all the experimental steps, the Mn $L_{2,3}$-edge NEXAFS spectra were continuously acquired; thus, we had enough spectra to perform a linear combination data analysis, and we were able to follow Mn electronic structure modifications as a function of temperature. We fitted the Mn L-edge NEXAFS spectra making linear combinations of well-defined reference manganese oxide spectra[49−51] as basis functions, according to the following formula:[52]

$$\text{fitted spectrum} = a\cdot MnO_2 + b\cdot Mn_2O_3 + c\cdot MnO$$

Thus, the concentration of the different oxidation states of Mn can be obtained as follows:

$$\%MnO_2 = \frac{a}{(a+b+c)}$$

$$\%Mn_2O3 = \frac{b}{(a+b+c)}$$

$$\%MnO = \frac{c}{(a+b+c)}$$

where *a*, *b*, and *c* are coefficients ranging from 0 to 1 depending on the different Mn(*x*) contents.

The electrochemical characterization of the fuel cells was carried out using the EIS (electrochemical impedance spectroscopy) technique. Data were collected with an AMEL 7200 frequency response analyzer and an AMEL 7050 potentiometer. The applied excitation voltage was 10 mV, and the range of frequencies analyzed was 10^6–10^{-1} Hz. The impedance spectra were registered first in hydrogen (20% in N_2) in a double-chamber configuration; then, the anode was exposed to several

https://doi.org/10.1021/acsaem.2c00163
ACS Appl. Energy Mater. 2022, 5, 6687−6699

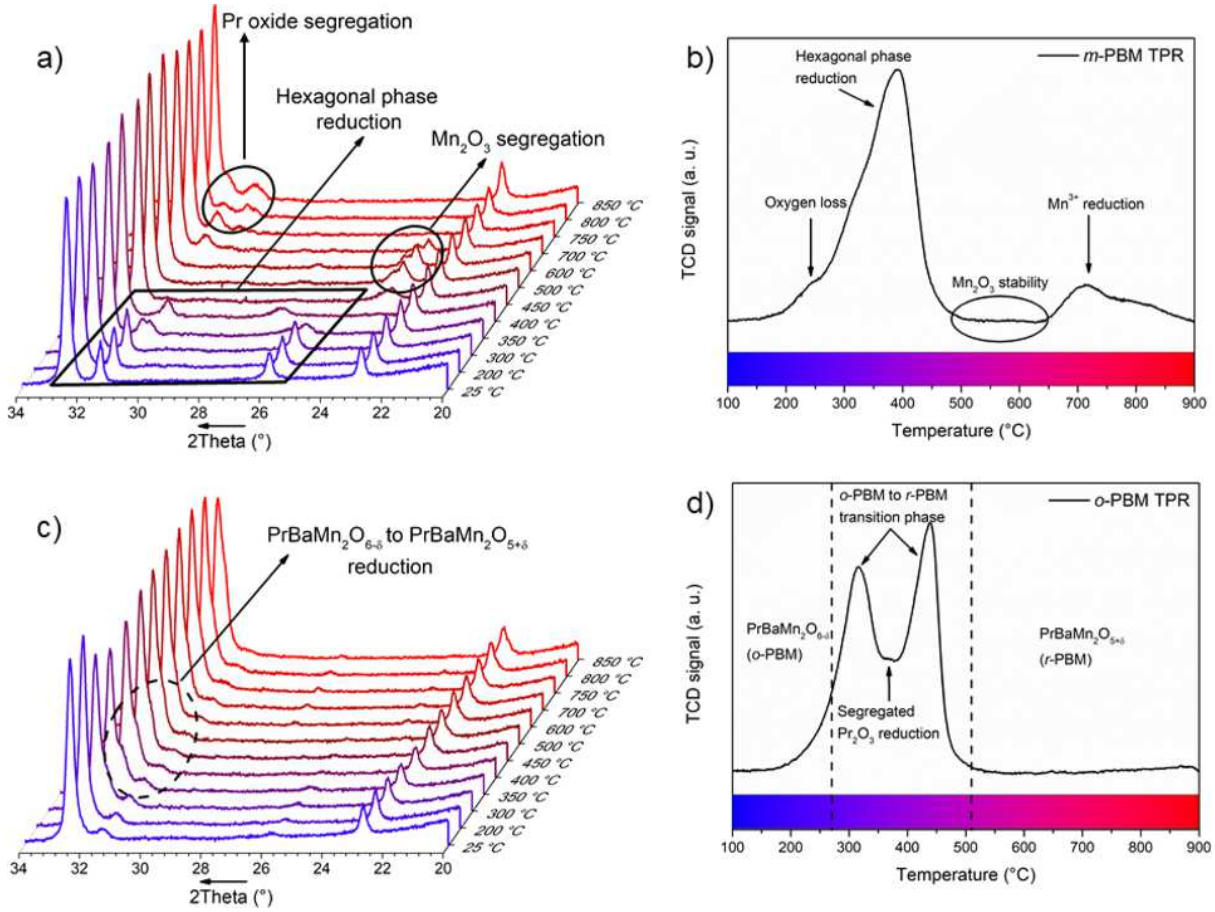

Figure 3. (a) Reactive HC-XRD spectra from 34 to 20° and (b) TPR profile of *m*-PBM to *r*-PBM reduction; (c) reactive HC-XRD spectra and (d) TPR profile of *o*-PBM to *r*-PBM reduction. In (a) and (c), diffractograms are reported from a higher angle to a lower angle to clearly show the decomposition of the hexagonal phase.

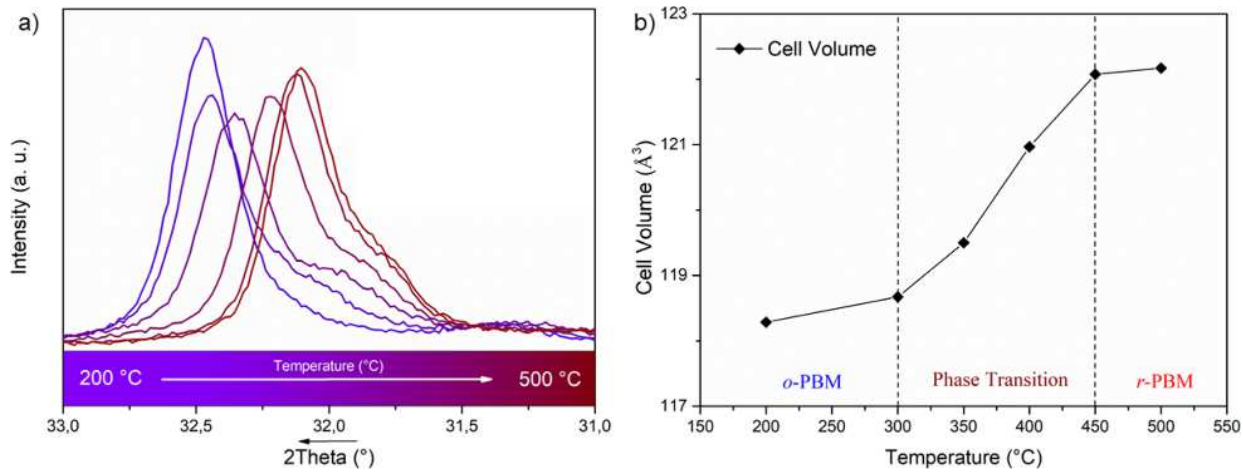

Figure 4. (a) HC-XRD spectral magnification from Figure 3c of the main peak of *o*-PBM from 33 to 31° between 200 and 500 °C and its angular position variation with the temperature; (b) variation of the cell volume as a function of *T*.

switches in reducing and oxidizing (air and CO_2) atmospheres at 850 °C.

RESULTS AND DISCUSSION

Figure 2 shows XRD patterns of the pristine $Pr_{0.5}Ba_{0.5}MnO_3$ (*m*-PBM) and the phases formed as an effect of its reduction and consequent oxidation at a high temperature. The *m*-PBM (black line) is constituted of two different structures, the cubic *c* ($Pm3m$) and the hexagonal *h* ($P6_3mc$);[34] both the oxidized phase $PrBaMn_2O_{6-\delta}$ (*o*-PBM, blue) and the reduced one $PrBaMn_2O_{5+\delta}$ (*r*-PBM, red) show instead the characteristic signals of $P4/mmm$ and $P4/nmm$ tetragonal phases, respectively.[44] These results are in good agreement with the literature.[45] The reduction of *m*-PBM (where Pr and Ba atoms

https://doi.org/10.1021/acsaem.2c00163
ACS Appl. Energy Mater. 2022, 5, 6687−6699

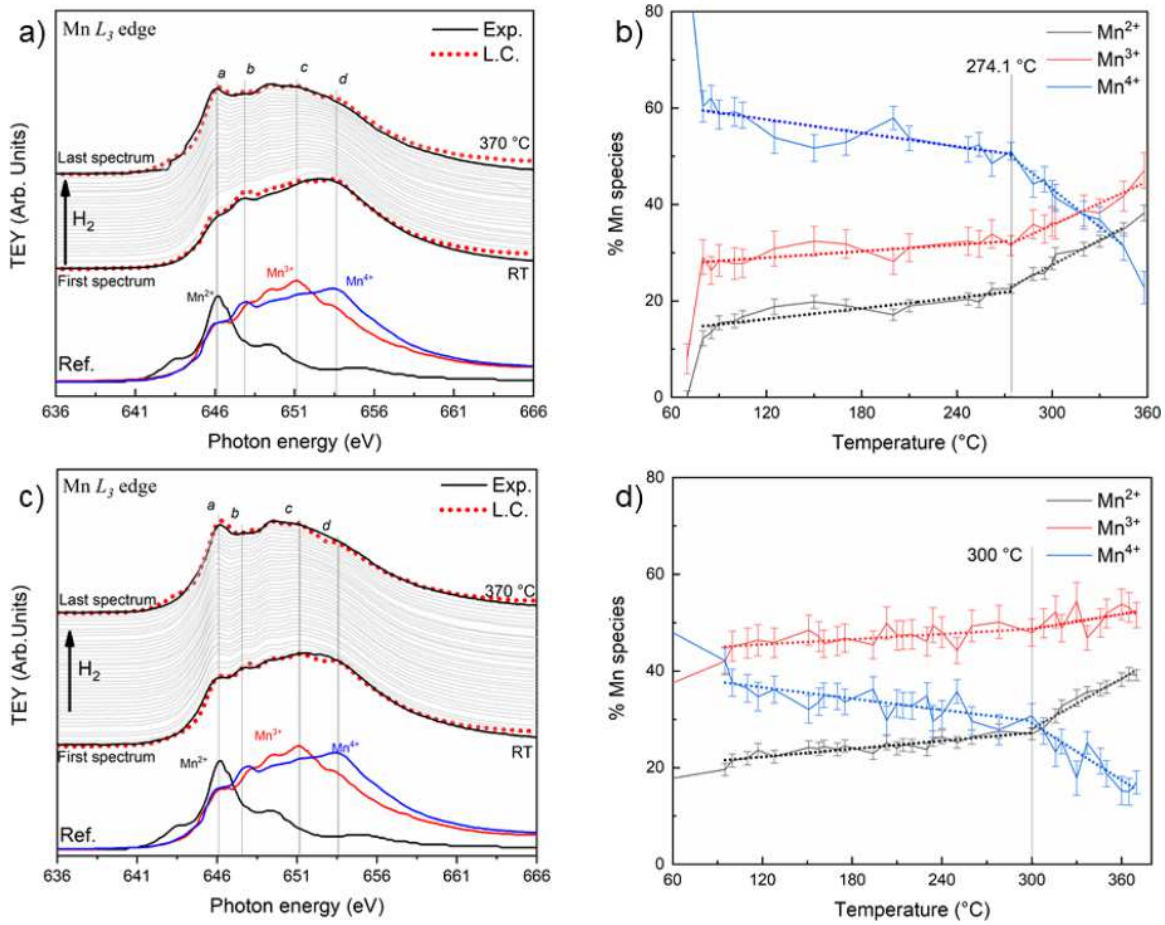

Figure 5. (a) *In situ* AP-NEXAFS spectral evolution of the Mn L_3 edge of *o*-PBM during the thermal treatment from RT to 370 °C in a reducing atmosphere of He (96%)/H_2 (4%). Black lines represent the acquired experimental spectra, while the red dotted lines are the result of the linear combination analysis obtained combining the three reference spectra of Mn^{2+} (black), Mn^{3+} (red), and Mn^{4+} (blue) reported in the bottom part of the figure. (b) Changing of the Mn oxidation state during the treatment of panel (a), obtained from the linear combination results, together with the calculated errors. (c,d) Respective NEXAFS and linear combination results obtained during a second thermal treatment in H_2 (4%), performed after the sample has been cooled down in an oxidizing mixture of He (96%)/O_2 (4%).

are stochastically disposed) leads to a reconstruction of the cubic *Pm*3*m* and the hexagonal $P6_3mc$ into a unique tetragonal layered structure, where A-site metals (Ba and Pr) settle onto alternated layers intercalated by [MnO_2] sublattices. It is reported[34] that the *r*-PBM phase can be obtained through a direct reduction of *m*-PBM powders in pure hydrogen at 850 °C. However, in this study, $PrBaMn_2O_{5+\delta}$ was obtained and stabilized at room temperature in two steps: (I) the reduction of *m*-PBM and its direct oxidation in air at 850 °C to form the oxidized phase $PrBaMn_2O_{6-\delta}$; (II) the reduction of this latter phase through a heating ramp up to 850 °C. This procedure prevented segregation of praseodymium oxide (Pr_2O_3) and manganese oxides. This phenomenon may happen if the layered structure is not yet stabilized, during the cooling phase of the reduced *m*-PBM (as observed in our first attempts, Figure S1), especially at medium-high temperatures, when instability of the Mn and Pr phases is observed[43] and Mn_2O_3 reduction and its gradual incorporation into the perovskite structure concur with the spill of Pr to form Pr_2O_3.

The direct oxidation of *r*-PBM at 850 °C did not cause a new disorder in the Pr and Ba cation disposition, and the layered structure of this phase seems to be maintained also in the oxidized phase (*o*-PBM). However, an enlargement of the peak and consequently an increase in the FWHM of the reduced structure can be observed in Figure 2b. This is attributed to the appearance of the (110) plane as a shoulder on the left of the peak, as well as to a higher presence of defects in the *r*-PBM, which is a less crystalline and more strained phase compared to the *o*-PBM phase.[44,45] Diffractograms of *o*-PBM and *r*-PBM also revealed a different angular position of their main peaks (32.5 and 32.3°, respectively), thus indicating that the two phases have different lattice cell dimensions, with a larger volume for the *r*-PBM. This expansion is due to an increase in the number of Mn^{3+}/Mn^{2+} couples and the concomitant formation of oxygen vacancies to keep electroneutrality during the reduction. A minor coordination of Pr and Mn ions and an increase in the length of Mn−O bonds lead to an increase in the tetragonality and an enlargement of the unit cell as reported in the literature.[44−46]

TEM analysis showed a similar morphology for all the three samples (Figure S2). Nanograins appear well-shaped, averaging in size hundreds of nanometers and with a tendency to agglomerate and form bigger coral-like structures. The nanograins appear strongly crystalline, showing defined spots in the SAED (selected-area electron diffraction) diffractogram. The pattern indexing and analysis are consistent with XRD data confirming the phase attributions at the nanoscale (Figures S3−S5 in the Supporting Information).

https://doi.org/10.1021/acsaem.2c00163
ACS Appl. Energy Mater. 2022, 5, 6687−6699

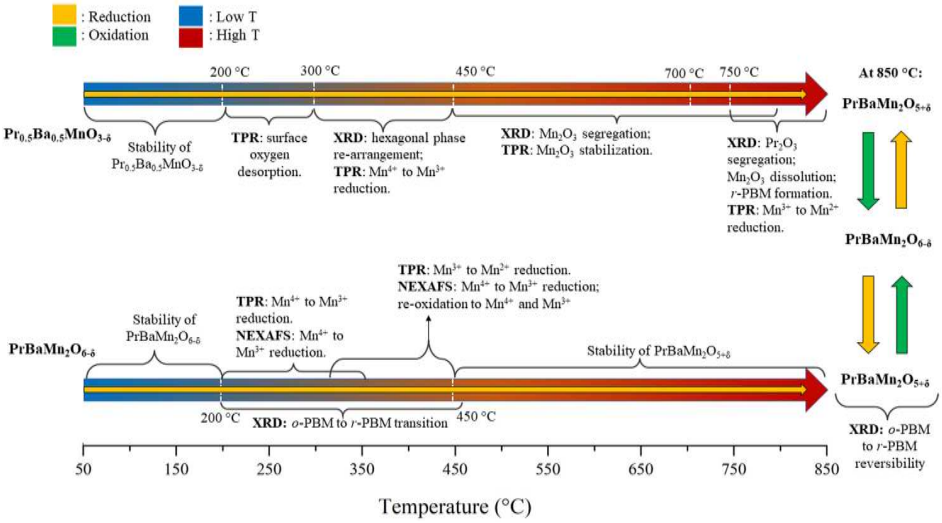

Figure 6. Summary of the main correlations between structural changes and redox behavior of PBM phases obtained by a multianalytical approach. Upper arrow: TPR and XRD results for the $Pr_{0.5}Ba_{0.5}MnO_3 \rightarrow PrBaMn_2O_{5+\delta}$ transformation involving a slow incorporation of the hexagonal phase into the perovskite structure and a temporary segregation of Mn species between 300 and 800 °C. Bottom arrow: TPR, XRD, and NEXAFS results for the transformation $PrBaMn_2O_{6-\delta} \rightarrow PrBaMn_2O_{5+\delta}$, which occurs with the reduction of Mn in two steps in the range of 200−450 °C, which is reversible at a high temperature.

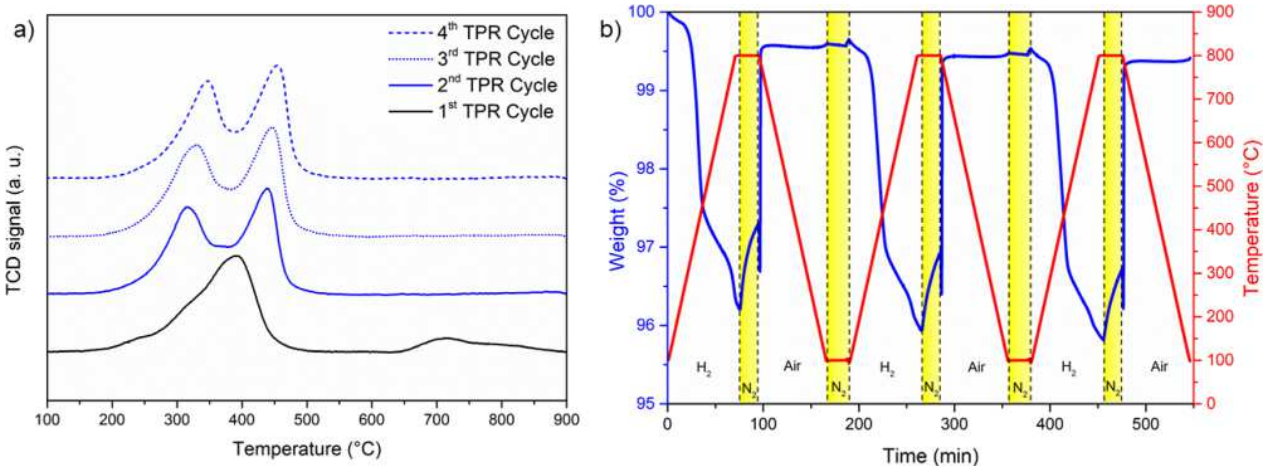

Figure 7. Consecutive cycles performed on a PBM sample in (a) TPR analysis and (b) TGA. Air was used as an oxidation agent.

Table 1. H_2 Consumption Values for Each TPR Cycle[a]

TPR cycle (no.)	T_{max} (°C)	H_2 consumption ($mmol_{H2} \cdot g^{-1}$)		reduction process
I	714	0.18	}1.53	hexagonal phase reduction
	390	1.35		Mn(III) → Mn(II)
II	316	1.05	}1.78	Mn(IV) → Mn(III)
	439	0.73		Mn(III) → Mn(II)
III	331	1.05	}1.78	Mn(IV) → Mn(III)
	446	0.73		Mn(III) → Mn(II)
IV	347	1.04	}1.79	Mn(IV) → Mn(III)
	455	0.75		Mn(III) → Mn(II)

[a]Hydrogen consumptions are calculated via deconvolution of the profiles.

Table 2. Thermogravimetric Weight Variation in % for Every Redox Cycle during Reduction and Consecutive Oxidation

TGA cycle (no.)	T_{max} first derivative (°C)	weight loss (reduction) (%)		weight increase (oxidation) (%)	oxidation grade (%)[a]
I	420	2.6	}3.8	3.4	99.6%
	803	1.2			
II	420	2.7	}3.8	3.4	99.8%
	500	0.9			
III	428	2.8	}3.8	3.6	99.8%
	501	0.9			

[a]The oxidation grade was calculated taking as a reference the previous cycle.

It has been recently reported[41] that the structural changes described above bring about peculiar redox properties in PBM phases. To investigate this in more detail, reactive hot-chamber XRD and TPR results (Figure 3) were combined to gain insights into the correlation between the structural evolution and the redox behavior in PBM perovskites. In Figure 3a, the selected angular range tracks the rearrangement from the cubic and the hexagonal structures to the layered phase, thanks to the modification of the main peak at 32.5° and the disappearance

https://doi.org/10.1021/acsaem.2c00163
ACS Appl. Energy Mater. 2022, 5, 6687−6699

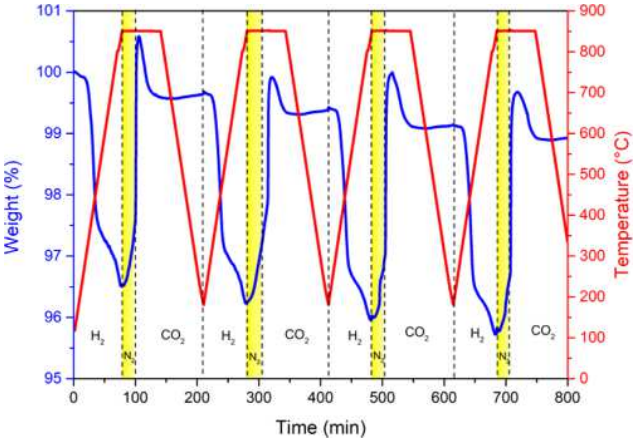

Figure 8. Consecutive SDT cycles performed on a PBM sample using CO_2 as an oxidating agent.

Table 3. Thermogravimetric Weight Variation in % for Every Redox Cycle during Reduction and Consecutive Oxidation in CO_2

SDT cycle (no.)	weight loss (reduction) (%)	weight increase (oxidation) (%)	oxidation grade (%)[a]	total oxidation grade (%)[b]
I	3.5	3.1	99.4%	
II	3.4	3.1	99.7%	98.9%
III	3.4	3.1	99.7%	
IV	3.2	3.1	99.9%	

[a]The oxidation grade was calculated with respect to the previous cycle, after the desorption phenomenon was visible immediately after CO_2 switch. [b]The total oxidation grade was calculated with respect to the % difference between the starting weight in cycle I and the final weight in cycle IV.

of the signals at 25.8 and 31.4°.[34,44] In the temperature range from 25 to 300 °C, no modification of the phase is visible, and only a small H_2 consumption peak appeared in the TPR profile at ~250 °C (Figure 3b), which is probably ascribable to a preliminary superficial oxygen desorption.[53] From 300 to 450 °C, we observed the disappearance of reflexes of the hexagonal phase in the diffractograms alongside a large H_2 consumption peak in the TPR profile. Intuitively, a preliminary, reduced layered structure is forming in this temperature range due to an initial reordering of Pr and Ba cations[54] and to the Mn^{4+} reduction to Mn^{3+}. At 450 °C, the formation of Mn^{3+} causes the segregation into different Mn_2O_3 species[55] (marked with a circle at ~23° in Figure 3a), which is a common phenomenon observed in manganite perovskites. Consequently, Mn_2O_3 is stable and detectable in the diffractograms at between 450 and 650 °C, and the TPR profile does not show any H_2 consumption. Manganese(III) oxide starts to decompose at 700 °C, which is the standard temperature[56,57] for the reduction of Mn^{3+} to Mn^{2+}. The ultimate inclusion of Mn(III) segregated species into the perovskite lattice ensues when the reduction to Mn(II) is completed at around 800 °C. Close to this temperature, the H_2 consumption profile declines until 900 °C (Figure 3b), and several peaks become visible between 28 and 30° (Figure 3a). They are associated to the initial stabilization of $PrBaMn_2O_{5+\delta}$, which then requires long isothermal calcination to be completed.[58] Pr_2O_3 was identified,[59] and a later measurement with a longer isotherm at 800 °C was carried out to verify its incorporation (Figure S6).

At the end of the reduction ramp, both the samples in the hot chamber and in the TPR reactor were maintained for 10 min in H_2 and then directly oxidized at 800 °C and cooled in air. The same XRD and TPR procedures were then repeated on the oxidized PBM (Figure 3c,d, respectively), leading to a significant difference in the results. The *in situ* X-ray acquisitions show a decrease in the amount of segregated Mn_2O_3 at temperatures higher than 500 °C and no other detectable segregations. Between 300 and 500 °C, the transition from the *o*-PBM to the *r*-PBM phase occurs (marked with a circle in Figure 3c). As mentioned before, this would cause an enlargement of the lattice cell,[61] which is detailed in Figure 4.

It is possible to see a notable variation in the angular position of the main peak (012) to lower angles (Figure 4a), which corresponds to an increment in the calculated cell volume of the structure (Figure 4b). From 200 to 300 °C, a relative shift of 3.0% in the angular position corresponds to a lattice thermal expansion of 0.4%. Between 300 and 450 °C, the relative peak position changes by 32.0%, compatibly with an increase in the volume of 2.8% and the formation of the larger $PrBaMn_2O_{5+\delta}$ lattice. The transformation is confirmed also by a simultaneous enlargement of the main peak and the appearance of a "shoulder" (attributable to the (110) plane), which is characteristic of the *r*-PBM phase.[60] There is also a decrease in peak intensity, which is compatible with a partial amorphization of the sample during the phase transition.[34,61] Between 450 and 500 °C, when the transition is completed, the angular shift is again due to the thermal expansion, and it drops by 2.0% (corresponding to a volume variation of 0.1%). The increase in the volume is straightforwardly correlated with the redox evolution of the material; meanwhile, the vacancy sublattice is enriched with defective sites (due to the Mn^{4+} to Mn^{3+} reduction), and the structure itself stretches due to the decrease in coordination of Mn cations.[44,49] When the proper amount of Mn^{3+} is formed, the entire lattice is large enough to permit the reduction to Mn^{2+} and the release of the last excess of oxygen to form $PrBaMn_2O_{5+\delta}$.

Figure 3d clearly shows that the *o*-PBM → *r*-PBM transition happens in association with a two-step reduction. Since no metastable or intermediate phases were observed during the *in situ* diffraction experiment, both the reduction steps are attributable to the reduction of *o*-PBM to *r*-PBM. Plausibly, the first TPR peak (at 320 °C) is related to the reduction of Mn^{4+} to Mn^{3+} in the $PrBaMn_2O_{6-\delta}$. Indeed, the direct reoxidation of reduced *r*-PBM (at 800 °C in the first redox cycle) is expected to turn a large amount of Mn^{3+} and Mn^{2+} into Mn^{4+}. The oxidation to Mn^{4+} is kinetically favored by the high temperature and by the enlarged lattice of *r*-PBM, through which oxygen can easily migrate.[62,63] Moreover, in manganite perovskites, the reduction of Mn^{4+} to Mn^{3+} is typically observed in this temperature range.[64] The second peak, at a higher temperature (420 °C), could instead be explained by a substantial anticipation of the reduction of Mn^{3+} owing to the higher mobility of oxygen in the layered structure of *o*-PBM.[41] The second reduction step proceeds until the equilibrium ratio between Mn^{3+}, Mn^{2+}, and oxygen vacancies is reached, at approximately 500 °C.

To support our hypothesis, the Mn species were investigated via *in situ* AP-NEXAFS characterization of *o*-PBM. The spectra of Mn $L_{2,3}$ edges were acquired continuously, at ambient pressure, exposing the sample to a mixture of He (96%)/H_2 (4%) and heating from room temperature to 370 °C. Then, the sample was cooled down to RT in an oxidizing atmosphere (He

https://doi.org/10.1021/acsaem.2c00163
ACS Appl. Energy Mater. 2022, 5, 6687−6699

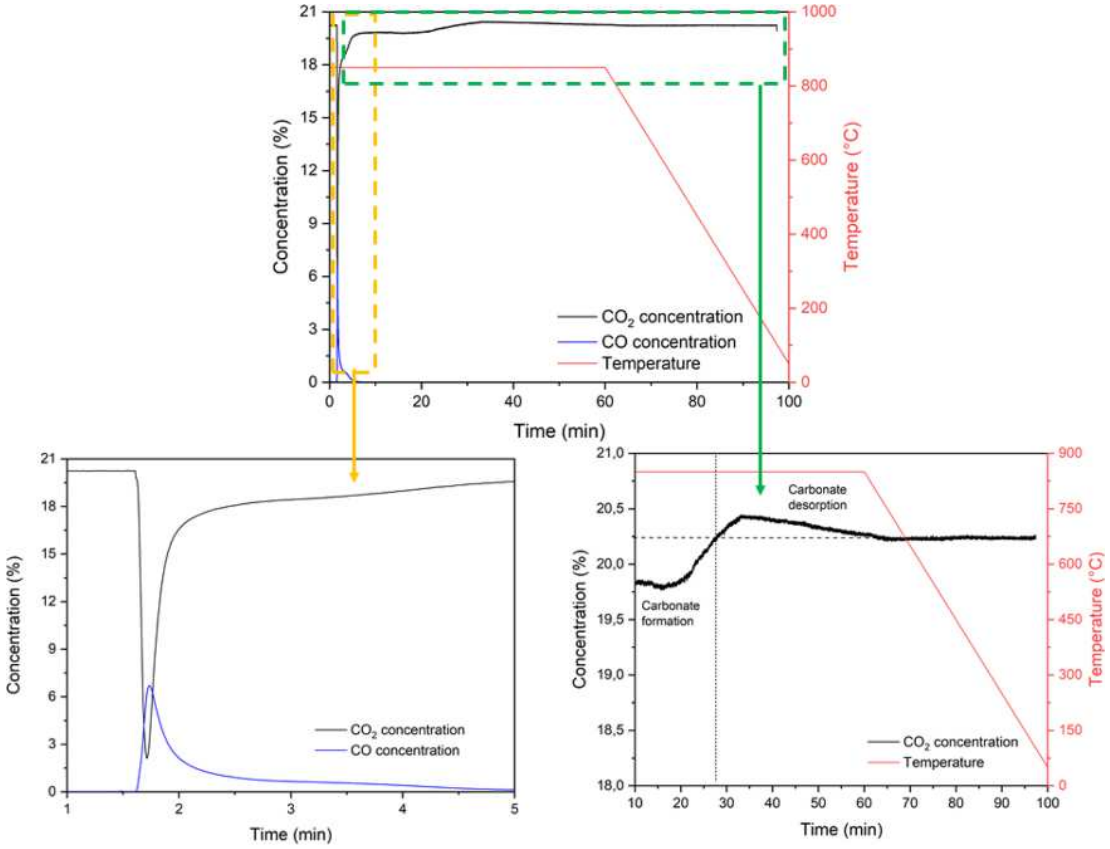

Figure 9. Mass spectroscopy analysis of CO_2 and CO during one cycle; in the magnification on the left, the concentration contribution of CO (blue) after the injection of CO_2 (black) in the reactor; on the right, the isotherm and the cooling ramp in CO_2.

Table 4. Mass Spectroscopy Analysis during the Oxidation of *r*-PBM with CO_2 and a Consecutive TPD in N_2[a]

CO_2 adsorption (mmol·g^{-1})	CO production (mmol·g^{-1})	CO_2 desorption isotherm (mmol·g^{-1})	CO_2 desorption TPD (mmol·g^{-1})
4.69	1.78	1.46	0.83

[a]The quantities are calculated from integration of the curves.

(96%)/O_2 (4%)), to investigate the Mn redox behavior. After that, a second thermal treatment in He (96%)/H_2 (4%) up to 370 °C was performed.

Figure 5 reports the results obtained for the two thermal treatments in a reducing atmosphere. Figure 5a,b refers to the first series, while panels (c) and (d) to the second. The electronic transitions giving rise to the most intense structures of the spectra of Figure 5 are related to dipole-allowed 2p → 3d transitions. In the figure, we focused our attention only on the L_3 edge since it is the one with more identifiable spectral changes. Looking at Figure 5a, a substantial modification of the Mn L_3 edge during the treatment is observable. The first spectrum, acquired at room temperature, is made of four main structures labeled as *a* (646.1 eV), *b* (647.8 eV), *c* (651.1 eV), and *d* (653.6 eV). Performing a linear combination of reference spectra of MnO, Mn_2O_3, and MnO_2,[65] we were able to assign structure *a* to Mn^{2+}, *b* and *c* to Mn^{3+}, and *d* to Mn^{4+}. The fitted spectrum is labeled with a dotted red line. From the linear combination fitting, we obtained the relative concentrations of the species, reported in Figure 5c. At 70 °C, the relative concentrations of Mn^{4+}, Mn^{3+}, and Mn^{2+} resulted to be respectively 60, 30, and 10%. These values confirm the presence of a prevalent *o*-PBM phase, which should be constituted mainly by Mn^{4+} and Mn^{3+} species. As we increased the temperature, we observed an increase in Mn^{3+} and Mn^{2+} contents together with decreasing of Mn^{4+}, confirming the Mn reduction, up to 274 °C. At this temperature, we observed a change in the reduction rate, indicating that Mn^{4+} is reduced more easily than before. These results are in perfect agreement with the TPR curve of Figure 3d, where we observed the first maximum in the Mn reduction rate at a temperature between 250 and 300 °C. The last spectrum, acquired at 370 °C, shows Mn^{4+}, Mn^{3+}, and Mn^{2+} contents of respectively ≈ 20, 50, and 30%, confirming that the first TPR peak of Figure 2d is linked to the occurrence of a partial phase transition from *o*-PBM to *r*-PBM. It must be considered that at 370 °C also, part of the second TPR peak contributes to the Mn reduction, so probably part of the 30% of Mn^{2+} comes from the reduction of Mn^{3+} → Mn^{2+} that occurs at the second TPR peak. Looking at the first spectrum acquired at room temperature of Figure 5c, we can see that a reoxidation occurred during the sample treatment in He (96%)/O_2 (4%). Indeed, from the linear combination results, we calculated Mn^{4+}, Mn^{3+}, and Mn^{2+} contents of respectively ≈ 40, 40, and 20%. The reoxidation, and thus the reversible formation, of the *o*-PBM phase was only partial and not total as measured in TPR and XRD analyses because the treatment in He (96%)/O_2 (4%) occurred at lower temperatures (360 °C vs 850 °C) and using lower concentrations of oxygen. The NEXAFS spectral series of Figure 5c shows that the second thermal treatment in He (96%)/H_2 (4%) again brings about a Mn reduction. This time, we detected a change in the reduction rate at 300 °C. At 370 °C, the Mn^{4+}, Mn^{3+}, and Mn^{2+} contents are respectively ≈ 10, 50, and 40%.

https://doi.org/10.1021/acsaem.2c00163
ACS Appl. Energy Mater. 2022, 5, 6687−6699

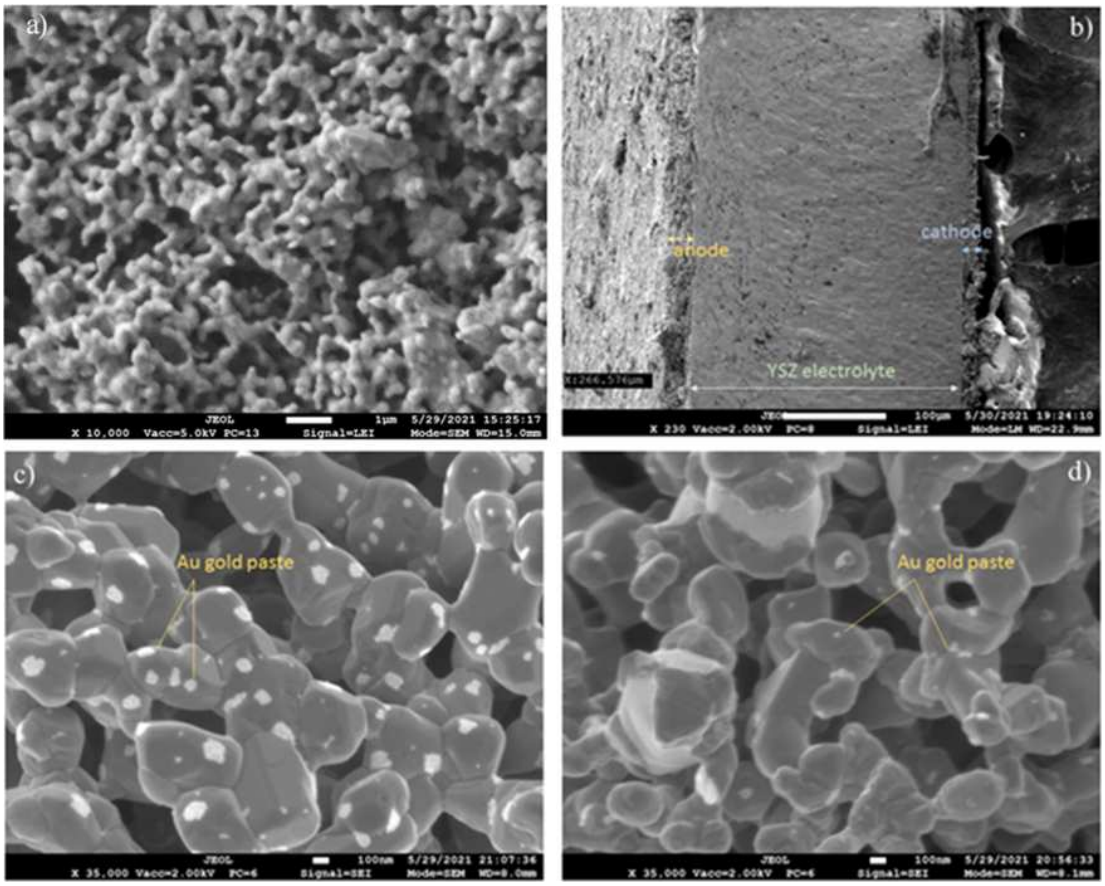

Figure 10. SEM images of PBM//YSZ//LSM: (a) $Pr_{0.5}Ba_{0.5}MnO_3$ anode before testing; (b) entire button cell before testing; (c) *o*-PBM anode after 8 redox cycles in air (last step: air); (d) *o*-PBM anode after 4 redox cycles in CO_2 (last step: CO_2).

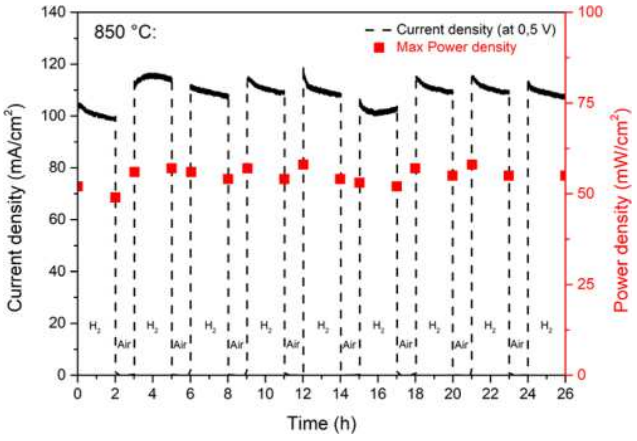

Figure 11. *r*-PBM//YSZ//LSM button cell performances in terms of current density at 0.5 V (black curve) and maximum power density (red squares) during 8 repeated redox cycles at 850 °C. Flow gases: 20% H_2 in N_2 (100 mL·min^{-1}) in the reducing steps and air (100 mL·min^{-1}) in the oxidizing steps. The maximum of power density was calculated from *I*−*V* polarization curves registred at the beginning and at the end of every reducing step (and it was always reached at ∼0.5 V).

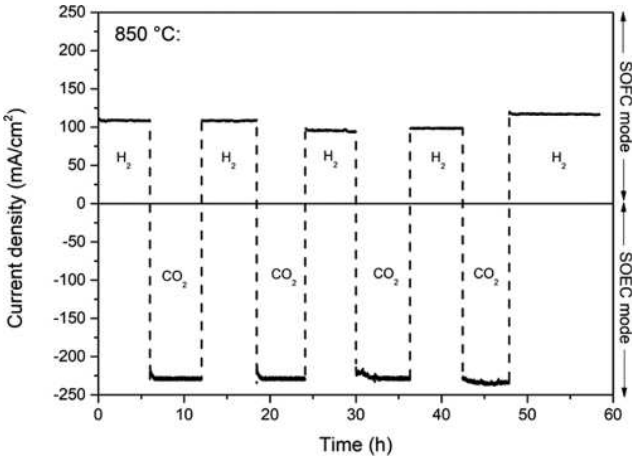

Figure 12. *r*-PBM//YSZ//LSM button cell performances in terms of current density (IUPAC convention) during 4 repeated H_2-SOFC/CO_2-SOEC cycles at 850 °C. Gas flow: 20% H_2 in N_2 (100 mL·min^{-1}) in the SOFC mode and 100% CO_2 flow (100 mL·min^{-1}) in the SOEC mode. Every cycle has a duration of 12 h (6 h in H_2 and 6 h in CO_2).

Comparing the values obtained at this temperature to the ones of the first series, there is the same amount of Mn^{3+}, a +10% amount of Mn^{2+}, and a −10% amount of Mn^{4+}. This is in line with the fact that Mn resulted in a more reduced state in the second treatment.

The combination of TPR analysis and NEXAFS characterization clearly confirms the reduction of both Mn^{4+} to Mn^{3+} and Mn^{3+} to Mn^{2+} of the *o*-PBM sample between 300 and 500 °C, where the phase transits from the oxidized layered form to the reduced one.

Figure 6 summarizes the main findings of XRD, TPR, and NEXAFS characterization highlighting the strong interplay

https://doi.org/10.1021/acsaem.2c00163
ACS Appl. Energy Mater. 2022, 5, 6687−6699

between the redox properties of PBM perovskite phases and their structural modification. For the first time, it was clearly demonstrated that the reduction of layered $PrBaMn_2O_{6-\delta}$ to the layered $PrBaMn_2O_{5+\delta}$ implies a reduction of Mn in two overlapping steps (first, Mn^{4+} to Mn^{3+} and then Mn^{3+} to Mn^{2+}). The reduction is completed at sensibly lower temperatures than that of mixed $Pr_{0.5}Ba_{0.5}MnO_3$, and it occurs with a stabilization of Mn^{2+} directly inside the lattice of layered structures, without the formation of segregated Mn_2O_3.

The reversibility of the *r*-PBM to *o*-PBM phase transition, along with the oxidation rate of $PrBaMn_2O_{5+\delta}$ in air, was investigated with several repeated TPR and TGA analyses (Figure 7a,b, respectively). TPR cycles confirm previous observations: from the second cycle, the profiles look similar, demonstrating the reversibility of the redox process for the layered phases. Table 1 reports the amount of H_2 consumed in each redox cycle. After the second cycle, there are no significant differences in the quantitative results and in the position of peaks. The deconvolution of TPR profiles successive to the first reduction (which are related to the transition from *o*-PBM to *r*-PBM) allows an approximate quantification of Mn species inside the *o*-PBM. In agreement with NEXAFS results, about 25% mole fraction of Mn is coordinated as Mn(IV) inside the lattice of *o*-PBM, and it reduces during the first step in Mn(III). Mn(III) is converted to Mn(II) in an amount of 17.5% in the second step of reduction.

The total amount of H_2 consumption remains almost constant in each step and in each cycle, meaning that the reduction/oxidation process is reversible and leads always to the same molar fractions of Mn(IV), Mn(III), and Mn(II).

Similar results were obtained in the thermogravimetric analyses (Figure 7b and Table 2). The derivative signals (wt %) of the first and the second thermogravimetric reduction (Figure S7a,b, respectively) have shapes comparable with the corresponding TPR profiles, except for some dissimilarities in the peak position (T_{max}) due to the different configurations of TGA and TPR analyzers. No significant changes are detectable between the second and the third TGA-redox cycle, denoting also in this case the reversibility of the phase transition. In addition, TGA analysis allows us to gain details in the process of oxidation. Figure 7b shows that the reoxidation of *r*-PBM to *o*-PBM at 800 °C takes place in a few seconds with restoration of the initial weight of 99.8%, meaning that the reoxidation of *r*-PBM is almost complete in our operating conditions. Table 2 shows that the loss and gain in weight for the layered structures are almost the same (in average 3.6%). Assuming that the loss/gain of weight is due to the release/uptake of oxygen of layered perovskites, we can evaluate that the oxygen nonstoichiometry in *r*-PBM is $\delta \sim -1$ (comparable to literature values[34,58]). On the basis of such substoichiometry, it is reasonable to estimate a Mn(III)/Mn(II) ratio of ~1 in *r*-PBM. Taking into account that in the second step of reduction, the total Mn(III) is reduced to less than 50% (only 17.5% from TPR results) and that the redox process is reversible, we can infer that Mn(II) is already present in the *o*-PBM phase, in agreement with NEXAFS analysis.

The quantitative estimations obtained from TPR and TGA analyses allow us to draw some conclusions on the mixed ionic and electronic conductivity of PBM layered perovskites:

- The low oxygen substoichiometry of *r*-PBM suggests that this phase has a high concentration of oxygen vacancies in the lattice, through which O^{2-} anions could migrate,[66] and therefore a high ionic conductivity.
- The copresence of Mn(III) and Mn(II) in both *r*-PBM and *o*-PBM structures should have a beneficial effect on their electronic conduction since the transport of e^- through the perovskite[16,66] is due to the coupling of different oxidation states of B-site cations.
- The reoxidation of *r*-PBM does not compromise the high number of redox couples in *o*-PBM, permitting appropriate electronic conductivity also in oxidative conditions.[41,67]

All the above observations suggest a possible employment of these oxides in SOFC and SOEC technology. In this perspective, to assess their potential application in CO_2 electrolysis, the redox behavior of PBM phases was investigated also using CO_2 as an oxidation agent.

Figure 8, together with Table 3, reports results of TGA cycles employing CO_2 as an oxidant. As it was observed for the experiments in air, the reoxidation of *r*-PBM to *o*-PBM occurs very rapidly. In addition, the gain in weight is beyond the initial value, which is probably due to the adsorption of CO_2 on the surface and the formation of carbonates on basic surface sites (Ba^{2+} and Pr^{3+}) of the perovskite.[60−62] Then, the weight slowly (40 min) decreases to a final recovery of 99.4% (99.6%, in air). To have information on the mechanism of CO_2 desorption, an analogous experiment was performed in the TPR equipment following the reactants and products during the isotherm measurement with a mass spectrometer. Figure 9 shows that the rapid gain in weight observed is attributable to a fast reoxidation of *r*-PBM, with production of CO in the first 5 min accompanied by a simultaneous adsorption of CO_2 on the surface. CO_2 continues to be adsorbed for almost 30 min and is then released with time without any CO production. Table 4 reports the quantitative analysis of the experiment: 38.0% reacted CO_2 (area below 20.2% in Figure 8) was converted to CO, and 31.1% was desorbed as CO_2 during the isotherm step at 800 °C, while no variations in concentration were registered during the cooling ramp. A further 17.7% was desorbed during a TPD analysis carried out in N_2, as shown in Figure S8. According to these results, CO_2 can easily oxidize *r*-PBM to *o*-PBM; however, the oxidation grade in CO_2 is lower than in air (98.8% vs 99.8%, respectively) due to possible formation of surface carbonates. Under our operating conditions, these latter species appeared unstable and only temporally adsorbed on the surface, thus not representing a severe limitation on redox cycles.

Such a behavior is crucial in all those applications of PBM perovskites where the environment is expected to be rich in CO_2, as for example the electrochemical conversion of carbon dioxide in an SOEC device or SOFCs fed by biogas.

PBM oxides were tested as electrode components under SOFC/SOEC operating conditions to assess the impact of their redox behavior on cell resistance against abrupt changes in the gas supply, which could occur during a malfunction or maintenance shutdown.

m-PBM//YSZ//LSM button cells were prepared as described in the experimental part and characterized through scanning electron microscopy (SEM) before and after being exposed to H_2/air or H_2/CO_2 redox cycles (Figure 10). Figure 10a,b shows the *m*-PBM electrode morphology after the sintering in air at 1100 °C, with micropores and macropores and round-shaped grains. Figure 10c,d evidences that the grain shape became rectangular/tetragonal after redox cycles, confirming the occurrence of the transition from the *m*-PBM to the *r*-PBM

https://doi.org/10.1021/acsaem.2c00163
ACS Appl. Energy Mater. 2022, 5, 6687−6699

phase (with a tetragonal structure) during the reduction conditions adopted for the cell testing.[34]

The endurance of the PBM layered electrode to several redox cycles is illustrated in Figure 11. No sensible variation in terms of delivered current density was registered during and at the end of the experiment. An average value of 109.3 $mA{\cdot}cm^{-2}$ was continuously measured during the reducing conditions, while the average maximum power density was 52.2 $mW{\cdot}cm^{-2}$. Further data in the performance of cells are provided in the Supporting Information (Figures S9 and S10). All results demonstrated that the electrode did not undergo significant mechanical strains and morphological reconstruction. Moreover, the transition from the oxidized to the reduced layered phase of PBM resulted in reversibility in SOFC operating conditions. Lattice expansions/contractions of these types of electrodes were compatible with the mechanical strength of the YSZ electrolyte prospecting a long-term redox resistance of cells. Similar results were obtained using CO_2 as a fuel and oxidant. Figure 12 shows the current density of the cell operating in an alternating SOFC/SOEC mode in pure H_2 or CO_2 at constant voltages of 0.5 and 1.5 V.

In this experiment, we assumed that CO_2 also performed as an oxidizing agent of the *r*-PBM phase since it was used pure and in excess. A small deactivation in the fuel cell mode was observable after the initial CO_2 exposure, in agreement with the results shown in Figure S10d. The small decrease in delivered current density could be attributable to the formation of surface carbonates, which may hinder the active sites for H_2 oxidation. However, the performance was recovered by the fourth cycle. Therefore, some sort of anode "hysteresis" can be assumed, which probably requires a longer period in the SOFC operation mode to restore the active surface PBM after CO_2 adsorption or numerous redox cycles for its complete regeneration. On the other hand, the activity toward CO_2 electrolysis was proven to be constant during the cycles. This behavior allows us to exclude the occurrence of irreversible degradation phenomena due to the formation of stable carbonates, at least under our test conditions, thus confirming the potential use of layered PBM oxides as electrode components of reversible SOEC systems. Further studies will be devoted to investigating the stability of the materials under different experimental conditions and atmospheres and for prolonged time. Following the methodology developed in this study, catalytic and electrocatalytic functionalities will also be implemented with different synthesis methods (coprecipitation, impregnation, and ball-milling) with the aim at studying the relationships between the activation at intermediate temperatures of C1 molecules (CH_4 and CO_2) and the redox properties of these materials.

CONCLUSIONS

This study gives insights into the redox properties of the layered phases $PrBaMn_2O_{5\pm\delta}$ (with $0 \le \delta \le 1$). These phases are formed from $Pr_{0.5}Ba_{0.5}MnO_{3-\delta}$ perovskite with a specific thermal redox treatment at high temperatures. Here, we demonstrate that the evolution of the PBM perovskite structure to a layered phase is accomplished by a different temperature-programmed reduction profile that could be considered diagnostic of a complete transition. NEXAFS studies demonstrated that the reduction of the layered oxidized phase $PrBaMn_2O_{6-\delta}$ occurs in two steps involving sequentially the redox couples Mn(IV)/Mn(III) and Mn(III)/Mn(II) at temperatures considerably lower than those reported for the conventional Mn-based perovskites. The process is reversible with fast kinetics of oxidation in different oxidizing atmospheres (air and CO_2) without structural changes of the layered structures and segregation of carbonates or other oxide phases. These findings pave the way for potential use of this class of oxides as oxygen carriers, promoters, and catalysts in several CO_2 valorization and H_2 production technologies.

Furthermore, this work demonstrates the importance of a multianalytical approach to characterize the functional properties of materials and to assess their potential fields of application.

ASSOCIATED CONTENT

Supporting Information

The Supporting Information is available free of charge at https://pubs.acs.org/doi/10.1021/acsaem.2c00163.

XRD patterns of *m*-PBM and *r*-PBM before oxidation; TEM images of PBM phases; TGA and CO_2-TPD measurements; OCV cycles in H_2/air and H_2/CO_2; EIS and *I*−*V* curves before and after oxidation steps in air or before and after SOFC/SOEC cycles (PDF)

AUTHOR INFORMATION

Corresponding Author

Marta Boaro − *Dipartimento Politecnico, University of Udine, Udine 33100, Italy;* orcid.org/0000-0002-6853-2965; Email: marta.boaro@uniud.it

Authors

Andrea Felli − *Dipartimento Politecnico, University of Udine, Udine 33100, Italy*

Silvia Mauri − *CNR-Istituto Officina dei Materiali, TASC, Trieste 34149, Italy; Dipartimento di Fisica, University of Trieste, Trieste 34127, Italy*

Marcello Marelli − *CNR-SCITEC, Istituto di Scienze e Tecnologie Chimiche "Giulio Natta", Milan 20138, Italy*

Piero Torelli − *CNR-Istituto Officina dei Materiali, TASC, Trieste 34149, Italy*

Alessandro Trovarelli − *Dipartimento Politecnico, University of Udine, Udine 33100, Italy;* orcid.org/0000-0002-1396-4031

Complete contact information is available at: https://pubs.acs.org/10.1021/acsaem.2c00163

Author Contributions

A.F. performed experimental work, conceptualization, and writing; S.M. and P.T. performed NEXAFS characterization; M.M. performed HRTEM characterization; A.T. performed manuscript editing and corrections; M.B. performed writing, conceptualization, and supervision of the project.

Notes

The authors declare no competing financial interest.

ACKNOWLEDGMENTS

Authors thank MIUR for funding (PRIN project-DIRECTBIO-SOFC, 2017FCFYHK, 2019−2022). Special thanks are also extended to Prof. Carla de Leitenburg (University of Udine, Polytechnical Department of Engineering and Architecture) for assistance during *in situ* XRD characterization.

REFERENCES

(1) Fang, J.; Gozgor, G.; Mahalik, M. K.; Padhan, H.; Xu, R. The Impact of Economic Complexity on Energy Demand in OECD Countries. *Environ. Sci. Pollut. Res.* **2021**, *28*, 33771−33780.

(2) Tschakert, P.; Waisman, H.; Abdul Halim, S.; Antwi-Agyei, P.; Dasgupta, P.; Hayward, B.; Kanninen, M.; Liverman, D.; Okereke, C.; Pinho, P.; Riahi, K.; Suarez, A. Chapter 5: Sustainable Development, Poverty Eradication and Reducing Inequalities. In: Global Warming of 1.5°C. An IPCC Special Report on the Impacts of Global Warming of 1.5°C above Pre-Industrial Levels and Related Global Gre. *IPCC Spec. Rep. Glob. Warm. 1.5 °C* 2018, 445−538.
(3) Badwal, S. P.; Giddey, S. S.; Munnings, C.; Bhatt, A. I.; Hollenkamp, A. F. Emerging Electrochemical Energy Conversion and Storage Technologies. *Front. Chem.* **2014**, *2*, 1−29.
(4) Abdalla, A. M.; Hossain, S.; Petra, P. M. I.; Ghasemi, M.; Azad, A. K. Achievements and Trends of Solid Oxide Fuel Cells in Clean Energy Field: A Perspective Review. *Front. Energy* **2020**, *14*, 359−382.
(5) Amiri, A.; Tang, S.; Steinberger-Wilckens, R.; Tadé, M. O. Evaluation of Fuel Diversity in Solid Oxide Fuel Cell System. *Int. J. Hydrogen Energy* **2018**, *43*, 23475−23487.
(6) Gandiglio, M.; De Sario, F.; Lanzini, A.; Bobba, S.; Santarelli, M.; Blengini, G. A. Life cycle assessment of a biogas-fed solid oxide fuel cell (SOFC) integrated in a wastewater treatment plant. *Energies* **2019**, *12*, 1611.
(7) Mehrpooya, M.; Sadeghzadeh, M.; Rahimi, A.; Pouriman, M. Technical Performance Analysis of a Combined Cooling Heating and Power (CCHP) System Based on Solid Oxide Fuel Cell (SOFC) Technology − A Building Application. *Energy Convers. Manage.* **2019**, *198*, 111767.
(8) da Silva, F. S.; de Souza, T. M. Novel Materials for Solid Oxide Fuel Cell Technologies: A Literature Review. *Int. J. Hydrogen Energy* **2017**, *42*, 26020−26036.
(9) Lyu, Y.; Xie, J.; Wang, D.; Wang, J. Review of Cell Performance in Solid Oxide Fuel Cells. *J. Mater. Sci.* **2020**, *55*, 7184−7207.
(10) Zhang, Y.; Knibbe, R.; Sunarso, J.; Zhong, Y.; Zhou, W.; Shao, Z.; Zhu, Z. Recent Progress on Advanced Materials for Solid-Oxide Fuel Cells Operating Below 500 °C. *Adv. Mater.* **2017**, *29*, 1−33.
(11) Ruiz-Morales, J. C.; Marrero-López, D.; Canales-Vázquez, J.; Irvine, J. T. S. Symmetric and Reversible Solid Oxide Fuel Cells. *RSC Adv.* **2011**, *1*, 1403−1414.
(12) Gómez, S. Y.; Hotza, D. Current Developments in Reversible Solid Oxide Fuel Cells. *Renew. Sustainable Energy Rev.* **2016**, *61*, 155−174.
(13) Mogensen, M. B.; Chen, M.; Frandsen, H. L.; Graves, C.; Hansen, J. B.; Hansen, K. V.; Hauch, A.; Jacobsen, T.; Jensen, S. H.; Skafte, T. L.; Sun, X. Reversible Solid-Oxide Cells for Clean and Sustainable Energy. *Clean Energy* **2019**, *3*, 175−201.
(14) Su, C.; Wang, W.; Liu, M.; Tadé, M. O.; Shao, Z. Progress and Prospects in Symmetrical Solid Oxide Fuel Cells with Two Identical Electrodes. *Adv. Energy Mater.* **2015**, *5*, 1500188.
(15) Peña, M. A.; Fierro, J. L. G. Chemical Structures and Performance of Perovskite Oxides. *Chem. Rev.* **2001**, *101*, 1981−2018.
(16) Hwang, J.; Rao, R. R.; Giordano, L.; Katayama, Y.; Yu, Y.; Shao-Horn, Y. Perovskites in Catalysis and Electrocatalysis. *Science* **2017**, *358*, 751−756.
(17) Irvine, J. T. S. Perovskite Oxide Anodes for SOFCs. In *Perovskite Oxide for Solid Oxide Fuel Cells*; Ishihara, T., Ed.; Springer US: Boston, MA, 2009; pp. 167−182.
(18) Sunarso, J.; Hashim, S. S.; Zhu, N.; Zhou, W. Perovskite Oxides Applications in High Temperature Oxygen Separation, Solid Oxide Fuel Cell and Membrane Reactor: A Review. *Prog. Energy Combust. Sci.* **2017**, *61*, 57−77.
(19) Afroze, S.; Karim, A.; Cheok, Q.; Eriksson, S.; Azad, A. K. Latest Development of Double Perovskite Electrode Materials for Solid Oxide Fuel Cells: A Review. *Front. Energy* **2019**, *13*, 770.
(20) Yin, W.-J.; Weng, B.; Ge, J.; Sun, Q.; Li, Z.; Yan, Y. Oxide Perovskites, Double Perovskites and Derivatives for Electrocatalysis, Photocatalysis, and Photovoltaics. *Energy Environ. Sci.* **2019**, *12*, 442−462.
(21) Bilal Hanif, M.; Motola, M.; qayyum, S.; Rauf, S.; Khalid, A.; Li, C.-J.; Li, C.-X. Recent Advancements, Doping Strategies and the Future Perspective of Perovskite-Based Solid Oxide Fuel Cells for Energy Conversion. *Chem. Eng. J.* **2022**, *428*, No. 132603.
(22) Kwon, O.; Joo, S.; Choi, S.; Sengodan, S.; Kim, G. Review on Exsolution and Its Driving Forces in Perovskites. *J. Phys. Energy* **2020**, *2*, No. 032001.
(23) Islam, Q. A.; Paydar, S.; Akbar, N.; Zhu, B.; Wu, Y. Nanoparticle Exsolution in Perovskite Oxide and Its Sustainable Electrochemical Energy Systems. *J. Power Sources* **2021**, *492*, No. 229626.
(24) Rahman, I. Z.; Raza, M. A.; Rahman, M. A. Perovskite Based Anode Materials for Solid Oxide Fuel Cell Application: A Review. *Adv. Mater. Res.* **2012**, *445*, 497−502.
(25) Lan, R.; Cowin, P. I.; Sengodan, S.; Tao, S. A Perovskite Oxide with High Conductivities in Both Air and Reducing Atmosphere for Use as Electrode for Solid Oxide Fuel Cells. *Sci. Rep.* **2016**, *6*, 4−11.
(26) Qiu, P.; Yang, X.; Wang, W.; Wei, T.; Lu, Y.; Lin, J.; Yuan, Z.; Jia, L.; Li, J.; Chen, F. Redox-Reversible Electrode Material for Direct Hydrocarbon Solid Oxide Fuel Cells. *ACS Appl. Mater. Interfaces* **2020**, *12*, 13988−13995.
(27) Marcucci, A.; Zurlo, F.; Sora, I. N.; Placidi, E.; Casciardi, S.; Licoccia, S.; Di Bartolomeo, E. A Redox Stable Pd-Doped Perovskite for SOFC Applications. *J. Mater. Chem. A* **2019**, *7*, 5344−5352.
(28) Zhou, J.; Xu, L.; Ding, C.; Wei, C.; Tao, Z. Layered Perovskite $(PrBa)_{0.95}(Fe_{0.9}Mo_{0.1})_2O_{5+\delta}$ as Electrode Materials for High-Performing Symmetrical Solid Oxide Electrolysis Cells. *Mater. Lett.* **2019**, *257*, No. 126758.
(29) Jin, F.; Li, J.; Wang, Y.; Chu, X.; Xu, M.; Zhai, Y.; Zhang, Y.; Fang, W.; Zou, P.; He, T. Evaluation of Fe and Mn Co-Doped Layered Perovskite $PrBaCo_{2/3}Fe_{2/3}Mn_{1/2}O_{5+\delta}$ as a Novel Cathode for Intermediate-Temperature Solid-Oxide Fuel Cell. *Ceram. Int.* **2018**, *44*, 22489−22496.
(30) Anjum, U.; Vashishtha, S.; Sinha, N.; Haider, M. A. Role of Oxygen Anion Diffusion in Improved Electrochemical Performance of Layered Perovskite $LnBa_{1-y}Sr_yCo_{2-x}Fe_xO_{5+\delta}$ (Ln=Pr, Nd, Gd) Electrodes. *Solid State Ionics* **2015**, *280*, 24−29.
(31) Lim, C.; Sengodan, S.; Jeong, D.; Shin, J.; Kim, G. Investigation of the Fe Doping Effect on the B-Site of the Layered Perovskite $PrBa_{0.8}Ca_{0.2}Co_2O_{5+\delta}$ for a Promising Cathode Material of the Intermediate-Temperature Solid Oxide Fuel Cells. *Int. J. Hydrogen Energy* **2019**, *44*, 1088−1095.
(32) He, W.; Wu, X.; Dong, F.; Ni, M. A Novel Layered Perovskite Electrode for Symmetrical Solid Oxide Fuel Cells: $PrBa(Fe_{0.8}Sc_{0.2})_2O_{5+\delta}$. *J. Power Sources* **2017**, *363*, 16−19.
(33) Li, F.; Tao, Z.; Dai, H.; Xi, X.; Ding, H. A High-Performing Proton-Conducting Solid Oxide Fuel Cell with Layered Perovskite Cathode in Intermediate Temperatures. *Int. J. Hydrogen Energy* **2018**, *43*, 19757−19762.
(34) Sengodan, S.; Choi, S.; Jun, A.; Shin, T. H.; Ju, Y. W.; Jeong, H. Y.; Shin, J.; Irvine, J. T. S.; Kim, G. Layered Oxygen-Deficient Double Perovskite as an Efficient and Stable Anode for Direct Hydrocarbon Solid Oxide Fuel Cells. *Nat. Mater.* **2015**, *14*, 205−209.
(35) Chen, D.; Wang, J.; Zhang, Z.; Shao, Z.; Ciucci, F. Boosting Oxygen Reduction / Evolution Reaction Activities with Layered Perovskite Catalysts. *Chem. Commun.* **2016**, *52*, 10739−10742.
(36) Bahout, M.; Managutti, P. B.; Dorcet, V.; Le Gal La Salle, A.; Paofai, S.; Hansen, T. C. In Situ Exsolution of Ni Particles on the $PrBaMn_2O_5$ SOFC Electrode Material Monitored by High Temperature Neutron Powder Diffraction under Hydrogen. *J. Mater. Chem. A* **2020**, *8*, 3590−3597.
(37) Joo, S.; Kwon, O.; Kim, K.; Kim, S.; Kim, H.; Shin, J.; Jeong, H. Y.; Sengodan, S.; Han, J. W.; Kim, G. Cation-Swapped Homogeneous Nanoparticles in Perovskite Oxides for High Power Density. *Nat. Commun.* **2019**, *10*, 1−9.
(38) Joo, S.; Kwon, O.; Kim, S.; Jeong, H. Y.; Kim, G. Ni-Fe Bimetallic Nanocatalysts Produced by Topotactic Exsolution in Fe Deposited $PrBaMn_{1.7}Ni_{0.3}O_{5+\delta}$ for Dry Reforming of Methane. *J. Electrochem. Soc.* **2020**, *167*, 64518.
(39) Li, N.; Luo, J.; Jia, L.; Pu, J.; Chi, B.; Li, J. Ni-Exsolved $PrBaMn_{2-X}Ni_xO_{6-\delta}$−Based Catalysts for High Performance of Ethanol Steam Reforming. *Mater. Today Energy* **2020**, *18*, No. 100512.
(40) Kim, K.; Joo, S.; Huang, R.; Kim, H. J.; Kim, G.; Han, J. W. Mechanistic Insights into the Phase Transition and Metal Ex-Solution

https://doi.org/10.1021/acsaem.2c00163
ACS Appl. Energy Mater. 2022, 5, 6687−6699

Phenomena of $Pr_{0.5}Ba_{0.5}Mn_{0.85}Co_{0.15}O_{3-\delta}$ from Simple to Layered Perovskite under Reducing Conditions and Enhanced Catalytic Activity. *Energy Environ. Sci.* **2021**, *14*, 873−882.
(41) Kudyakova, V. S.; Politov, B. V.; Chukin, A. V.; Markov, A. A.; Suntsov, A. Y.; Kozhevnikov, V. L. Phase Stability and Oxygen Storage Capacity of $PrBaMn_2O_{6-\delta}$. *Mater. Lett.* **2020**, *269*, No. 127650.
(42) Jeamjumnunja, K.; Gong, W.; Makarenko, T.; Jacobson, A. J. A Determination of the Oxygen Non-Stoichiometry of the Oxygen Storage Materials $LnBaMn_2O_{5+\delta}$ (Ln=Gd, Pr). *J. Solid State Chem.* **2016**, *239*, 36−45.
(43) Felli, A.; Trovarelli, A.; Boaro, M. Investigation of the Redox Behaviour of Double Perovskite $PrBaMn_2O_{5+\delta}$. *ECS Trans.* **2021**, *103*, 1479.
(44) Shin, T. H.; Myung, J.-H.; Verbraeken, M.; Kim, G.; Irvine, J. T. S. Oxygen Deficient Layered Double Perovskite as an Active Cathode for CO_2 Electrolysis Using a Solid Oxide Conductor. *Faraday Discuss.* **2015**, *182*, 227−239.
(45) Trukhanov, S. V.; Troyanchuk, I. O.; Hervieu, M.; Szymczak, H.; Bärner, K. Magnetic and Electrical Properties of $LBaMn_2O_{6-y}$ (L=Pr, Nd, Sm, Eu, Gd, Tb) Manganites. *Phys. Rev. B* **2002**, *66*, No. 184424.
(46) Nakajima, T.; Kageyama, H.; Yoshizawa, H.; Ohoyama, K.; Ueda, Y. Ground State Properties of the A-Site Ordered Manganites, $RBaMn_2O_6$ (R = La, Pr and Nd). *J. Phys. Soc. Jpn.* **2003**, *72*, 3237−3242.
(47) Jain, A.; Ong, S. P.; Hautier, G.; Chen, W.; Richards, W. D.; Dacek, S.; Cholia, S.; Gunter, D.; Skinner, D.; Ceder, G.; Persson, K. A. Commentary: The Materials Project: A Materials Genome Approach to Accelerating Materials Innovation. *APL Mater.* **2013**, *1*, No. 011002.
(48) Castán-Guerrero, D.; Krizmancic, D.; Bonanni, V.; Edla, R.; Deluisa, A.; Salvador, F.; Rossi, G.; Panaccione, G.; Torelli, P.; Krizmancic, D.; Bonanni, V.; Edla, R.; Deluisa, A.; Salvador, F. A Reaction Cell for Ambient Pressure Soft X-Ray Absorption Spectroscopy A Reaction Cell for Ambient Pressure Soft x-Ray Absorption Spectroscopy. *Rev. Sci. Instrum.* **2018**, *89*, No. 054101.
(49) Liu, Y.; Wang, Z.; Veder, J.-P. M.; Xu, Z.; Zhong, Y.; Zhou, W.; Tade, M. O.; Wang, S.; Shao, Z. Highly Defective Layered Double Perovskite Oxide for Efficient Energy Storage via Reversible Pseudocapacitive Oxygen-Anion Intercalation. *Adv. Energy Mater.* **2018**, *8*, 1702604.
(50) Mette, K.; Bergmann, A.; Tessonnier, J.; Hävecker, M.; Yao, L.; Ressler, T.; Schlögl, R.; Strasser, P.; Behrens, M. Nanostructured Manganese Oxide Supported on Carbon Nanotubes for Electrocatalytic Water Splitting. *ChemCatChem* **2012**, *4*, 851−862.
(51) Saywell, A.; Magnano, G.; Satterley, C. J.; Perdigão, L. M. A.; Britton, A. J.; Taleb, N.; del Carmen Giménez-López, M.; Champness, N. R.; O'Shea, J. N.; Beton, P. H. Self-Assembled Aggregates Formed by Single-Molecule Magnets on a Gold Surface. *Nat. Commun.* **2010**, *1*, 75.
(52) Xi, L.; Schwanke, C.; Xiao, J.; Abdi, F. F.; Zaharieva, I.; Lange, K. M. In Situ L-Edge XAS Study of a Manganese Oxide Water Oxidation Catalyst. *J. Phys. Chem. C* **2017**, *121*, 12003−12009.
(53) Hua, B.; Sun, Y.; Zhang, Y.; Hua, B.; Behnamian, Y.; Li, J.; Cui, S. Molybdenum Doped $Pr_{0.5}Ba_{0.5}MnO_{3-\delta}$ (Mo-PBMO) Double Perovskite as a Potential Solid Oxide Fuel Cell Anode Material. *J. Power Sources* **2016**, *301*, 237−241.
(54) Choi, S.; Sengodan, S.; Park, S.; Ju, Y.-W.; Kim, J.; Hyodo, J.; Jeong, H. Y.; Ishihara, T.; Shin, J.; Kim, G. A Robust Symmetrical Electrode with Layered Perovskite Structure for Direct Hydrocarbon Solid Oxide Fuel Cells: $PrBa_{0.8}Ca_{0.2}Mn_2O_{5+\delta}$. *J. Mater. Chem. A* **2016**, *4*, 1747−1753.
(55) Zhang, X.; Li, H.; Hou, F.; Yang, Y.; Dong, H.; Liu, N.; Wang, Y.; Cui, L. Synthesis of Highly Efficient Mn_2O_3 Catalysts for CO Oxidation Derived from Mn-MIL-100. *Appl. Surf. Sci.* **2017**, *411*, 27−33.
(56) Zhang-Steenwinkel, Y.; Beckers, J.; Bliek, A. Surface Properties and Catalytic Performance in CO Oxidation of Cerium Substituted Lanthanum−Manganese Oxides. *Appl. Catal., A* **2002**, *235*, 79−92.
(57) Ciambelli, P.; Cimino, S.; De Rossi, S.; Faticanti, M.; Lisi, L.; Minelli, G.; Pettiti, I.; Porta, P.; Russo, G.; Turco, M. AMnO3 (A=La, Nd, Sm) and $Sm_{1-x}Sr_xMnO_3$ Perovskites as Combustion Catalysts: Structural, Redox and Catalytic Properties. *Appl. Catal., B* **2000**, *24*, 243−253.
(58) Klimkowicz, A.; Świerczek, K.; Zheng, K.; Wallacher, D.; Takasaki, A. Oxygen Release from $BaLnMn_2O_6$ (Ln: Pr, Nd, Y) under Reducing Conditions as Studied by Neutron Diffraction. *J. Mater. Sci.* **2017**, *52*, 6476−6485.
(59) Yang, X.; Yang, L.; Lin, S.; Zhou, R. New Insight into the Doping Effect of Pr_2O_3 on the Structure−Activity Relationship of Pd/CeO_2−ZrO_2 Catalysts by Raman and XRD Rietveld Analysis. *J. Phys. Chem. C* **2015**, *119*, 6065−6074.
(60) Garcia-Garcia, F. J.; Sayagués, M. J.; Gotor, F. J. A Novel, Simple and Highly Efficient Route to Obtain $PrBaMn_2O_{5+\delta}$ Double Perovskite: Mechanochemical Synthesis. *Nanomaterials* **2021**, DOI: 10.3390/nano11020380.
(61) Krüger, H.; Kahlenberg, V.; Petříček, V.; Phillipp, F.; Wertl, W. High-Temperature Structural Phase Transition in $Ca_2Fe_2O_5$ Studied by in-Situ X-Ray Diffraction and Transmission Electron Microscopy. *J. Solid State Chem.* **2009**, *182*, 1515−1523.
(62) Chen, M.; Xu, X.; Bao, S.; Ren, G.-K.; Lin, Y.-H.; Jacobson, A. J.; Ma, J.; Nan, C.-W.; Chen, C. Remarkable Switching of Transport Properties and Surface Exchange Kinetics in Epitaxial $PrBaMn_2O_{5+\delta}$ Films. *Acta Mater.* **2020**, *186*, 517−522.
(63) Shrestha, P.; Nair, M. M.; Mahinpey, N. Isothermal Redox Cycling of A- and B-Site Substituted Manganite-Based Perovskites for CO_2 Conversion. *Can. J. Chem. Eng.* **2021**, *99*, S551−S561.
(64) Peron, G.; Glisenti, A. Perovskites as Alternatives to Noble Metals in Automotive Exhaust Abatement: Activation of Oxygen on LaCrO3 and LaMnO3. *Top. Catal.* **2019**, *62*, 244−251.
(65) Comno, L.; Fu, J.; Zhao, H.; Wang, J.; Shen, Y.; Liu, M. Preparation and Electrochemical Performance of Double Perovskite. *Int. J. Miner. Metall. Mater.* **2018**, *25*, 950−956.
(66) Teraoka, Y.; Zhang, H. M.; Okamoto, K.; Yamazoe, N. Mixed Ionic-Electronic Conductivity of $La_{1-x}Sr_xCo_{1-y}Fe_yO_{3-\delta}$ Perovskite-Type Oxides. *Mater. Res. Bull.* **1988**, *23*, 51−58.
(67) Kudyakova, V. S.; Shalamova, A. M.; Politov, B. V.; Suntsov, A. Y. Specific Interrelations of Magnetic, Thermodynamic and Structural Properties in Highly Non-Stoichiometric $PrBaMnFe_2O_{6-\delta}$ Double Perovskite. *J. Alloys Compd.* **2021**, *886*, 161133.

https://doi.org/10.1021/acsaem.2c00163
ACS Appl. Energy Mater. 2022, 5, 6687−6699